# Microstructure equilibration with consideration of elastic and interfacial interactions via quantum annealing with application to the solid electrolyte LLZO

Roland Sandt, Yann Le Bouar, Robert Spatschek

# Microstructure equilibration with consideration of elastic and interfacial interactions via quantum annealing with application to the solid electrolyte LLZO

Roland Sandt,[1] Yann Le Bouar,[2] and Robert Spatschek[1,3]
[1]*Structure and Function of Materials, Institute of Energy and Climate Research IEK-2, Forschungszentrum Jülich GmbH, 52425 Jülich, Germany*
[2]*Université Paris-Saclay, ONERA, CNRS, Laboratoire d'Etude des Microstructures, 92320 Châtillon, France*
[3]*JARA-ENERGY, 52425 Jülich, Germany*

(Received 3 May 2024; accepted 5 June 2024; published 10 July 2024)

We present a detailed derivation of the elastic energy of a homogeneous, isotropic linear elastic medium consisting of different coherent martensite variants or phases and its mapping to an Ising model, as required for an efficient quantum annealing determination of the equilibrium microstructure. The approach is demonstrated for a sample with a large number of grains with a tetragonal eigenstrain. Furthermore, we illustrate how the elastic effects may lead to the formation of ion conducting channels in the doped solid electrolyte $Li_7La_3Zr_2O_{12}$ (LLZO). Apart from bulk elastic and chemical effect we demonstrate how to include interfacial effects into the quantum annealing approach and emphasize the importance of high precision elastic calculations.

DOI: 10.1103/PhysRevResearch.6.033047

## I. INTRODUCTION

The properties of many materials are strongly influenced by the microstructure, which can ideally be tailored to lead to the desired behavior as needed for the intended application. Here, mechanical effects can trigger solid state transformations, which could be used to create the desired microstructure. Such a processing technology needs to come along with powerful simulation techniques, which are able to quantitatively predict equilibrated microstructures in large and application relevant systems, to ensure a long term stability of the adjusted phase arrangement. Whereas phase-field approaches [1–4] are strong and established approaches to simulate the kinetics of microstructure evolution, the long-term behavior involving thermochemical, interfacial but also mechanical effects is hard to address due to large simulation times.

Recently, we established a new simulation technique which is based on quantum annealing (QA), and which allows to directly determine the thermodynamic ground state for a martensitic microstructure with elastic interactions in a very efficient way [5,6]. QA itself is a specific case of adiabatic quantum computing, which has become very powerful during recent years [7–11]. Nowadays such machines with several thousand qubits and couplers are available on the market. To use this technique, it is necessary to express the problem of interest as a discrete optimization problem, as described through an Ising model or equivalently through a quadratic unconstrained binary optimization problem [12–14]. Despite the fact that quantum annealers allow highly efficient global energy minimizations, applications of this technology in the field of materials science and related disciplines [5,15–25] are still rare due to this specific problem structure. The main part of actual research concentrates on performance test and benchmarking of quantum annealing versus classical algorithms [26–29]. Indeed, the solution of optimization problems via quantum annealing plays recently a role in other research fields [30–35].

The problem and solution approach proposed in Refs. [5,6] is based on the concept that a grain structure of the material of interest is known, and that for each grain by the selection of a martensite variant (or more generally a phase) is driven by the minimization of energy. Such transformations are important for example for shape memory alloys, which undergo reversible, structural phase transitions between martensitic and austenitic phases, depending on temperature and the trained, previous shape [36,37]. If the grains are coherently connected, then interfaces between different phases lead to internal stresses and therefore raise the elastic energy. The approach expresses the energy minimization as a discrete optimization process by mapping it to a spin glass problem [38–41]. Although this is a significant simplification of the entire microstructure optimization process, the problem size grows exponentially with the number of grains and is therefore hard to solve with conventional computing methods. We have demonstrated in Ref. [5] that QA leads to a remarkable acceleration of the computations, therefore allowing for large scale simulations.

The purpose of the the present paper is fourfold:

First, it describes the entire methodology in more detail than in Ref. [5]. This includes in particular the derivation of the coefficients of the underlying spin glass model through a Fourier space representation of the elastic energy stored in the microstructure (Sec. II). In this way, one obtains explicit

expressions for the coefficients of the Ising model, as used by the quantum annealer. This approach has the advantage of delivering accurate expressions for the elastic interactions between the grains. As we demonstrate explicitly in this paper, this is a necessary condition for obtaining the correct equilibrium microstructures using QA (Sec. III D).

Second, we demonstrate the application to large systems with up to several thousand grains, which is important for generating representative volume elements of the entire microstructure and their response to external mechanical loads (Sec. III A).

Third, we apply the general approach to the ceramic solid electrolyte $Li_7La_3Zr_2O_{12}$ (LLZO), therefore going beyond the aforementioned shape memory alloys. LLZO has a thermodynamically stable tetragonal phase with poor Li-ion conductivity [42,43]. However, for battery applications the highly conductive and at ambient temperatures unstable cubic phases [42,44] is desired. The cubic phase can be stabilized via substitutions of different aliovalent elements like $Al^{3+}$, $Ta^{5+}$, and $Ga^{3+}$ [43–45]. Several studies investigated the resulting mechanical and structural properties of pure and substituted tetragonal and cubic phases [46–48]. Here we investigate to which extent percolating, highly conducting ion channels may form as a result from a self-organization process driven by elastic coherency stresses (Sec. III B).

Finally, we demonstrate how the approach can be extended to incorporate also interfacial effects and discuss their influence on the microstructure selection (Sec. III C).

## II. METHODS

### A. Elastic energy in reciprocal space

In this section an expression for the elastic energy of the system, based on the solution of the underlying elastic problem in reciprocal space, is presented. Although the use of Fourier methods is beneficial and allows to obtain the quantum annealer coefficients with sufficient accuracy, in principle any other elastic solver can be used as well, as discussed in Ref. [6]. For our specific application, we assume that the eigenstrain is constant within each grain (and related to the martensite variant), and that the grains are coherently connected. This means on the level of continuum elasticity that at the interfaces between adjacent grains not only the normal and shear stresses are continuous (by force balance) but also the displacements. For simplicity, we assume isotropic elasticity. As external boundary cases we consider the two important cases of either a vanishing mean stress in a periodic system or a given mean strain $\langle\epsilon_{\alpha\beta}\rangle$. Whereas the formalism works both in two and three dimensions, we use for the applications below specifically a two dimensional plane strain setup, i.e., the displacement component vanishes, $u_z \equiv 0$, and $u_x$, $u_y$ depend only on $x$ and $y$. From the obtained expression of the elastic energy we generate a formulation as Ising model, which can then be implemented on the quantum annealer. As we assume the elastic constants to be the same everywhere (homogeneous elasticity), the interactions between grains decompose into pairwise terms [49], which is necessary for the annealer formulation.

The starting point is the elastic energy for isotropic materials

$$E_{\mathrm{el}} = \int_V \left( \frac{\lambda}{2} \left(\epsilon_{\alpha\alpha}(\mathbf{r}) - \epsilon^{(0)}_{\alpha\alpha}(\mathbf{r})\right)^2 + \mu \left(\epsilon_{\alpha\beta}(\mathbf{r}) - \epsilon^{(0)}_{\alpha\beta}(\mathbf{r})\right)^2 \right) d\mathbf{r}, \tag{1}$$

with Lamé coefficient $\lambda$ and shear modulus $\mu$ (we employ Einstein's sum convention). $\epsilon^{(0)}_{\alpha\beta}(\mathbf{r})$ is the position-dependent eigenstrain, which is known for a given microstructure. After solution of the elastic problem, the elastic energy of the system reads in reciprocal space

$$\begin{aligned} E_{\mathrm{el}} = {} & \frac{V}{2} \sum_{\mathbf{k}\neq 0} \left[ \hat{\sigma}^{(0)*}_{\alpha\beta}(\mathbf{k}) \hat{\epsilon}^{(0)}_{\alpha\beta}(\mathbf{k}) - \hat{\sigma}^{(0)}_{\alpha\delta}(\mathbf{k}) k_\alpha G_{\delta\beta} k_\gamma \hat{\sigma}^{(0)*}_{\beta\gamma}(\mathbf{k}) \right] \\ & + \frac{\lambda V}{2} \left( \langle\epsilon_{\alpha\alpha}\rangle - \hat{\epsilon}^{(0)}_{\alpha\alpha}(\mathbf{k}=0) \right)^2 \\ & + \mu V \left( \langle\epsilon_{\alpha\beta}\rangle - \hat{\epsilon}^{(0)}_{\alpha\beta}(\mathbf{k}=0) \right)^2. \end{aligned} \tag{2}$$

For a derivation of this energy expression and explanation of the involved terms we refer to the Appendix. In particular, the hat symbol (ˆ) denotes Fourier transformation with reciprocal lattice vector $\mathbf{k}$, and $\sigma^{(0)}_{\alpha\beta} = \lambda\delta_{\alpha\beta}\epsilon^{(0)}_{\gamma\gamma} + 2\mu\epsilon^{(0)}_{\alpha\beta}$ is the eigenstress. The isotropic elastic Green tensor is defined through its inverse, $G^{-1}_{\beta\delta} = \lambda k_\beta k_\delta + \mu k_\alpha k_\alpha \delta_{\beta\delta} + \mu k_\beta k_\delta$. The expression (2) holds for given average strain boundary conditions [case (ii)]. For a stress free system [case (i)], where the average stress vanishes, the last two terms vanish, as by mechanical equilibrium conditions one obtains in particular for the homogeneous strain $\langle\epsilon_{\alpha\beta}\rangle = \hat{\epsilon}^{(0)}_{\alpha\beta}(\mathbf{k}=0)$.

### B. Ising formulation

We assume the entire system to be decomposed into $N$ grains. At this point, we do not make assumptions about the grain structure, so they can be, e.g., regular cuboids or random structures, e.g., taken from electron backscatter diffraction (EBSD) images or a Voronoi tesselation. In agreement with the preceding analysis, the grains are assumed to be coherent from the point of view of elasticity. The grains are enumerated by $n$ and characterized by an indicator function

$$\theta_n(\mathbf{r}) = \begin{cases} 1 & \text{inside grain } n, \\ 0 & \text{otherwise}, \end{cases} \tag{3}$$

which satisfies the condition $\sum_i \theta_i(\mathbf{r}) = 1$. The eigenstrain therefore reads

$$\begin{aligned} \epsilon^{(0)}_{\alpha\beta}(\mathbf{r}) &= \sum_{n=1}^{N} \theta_n(\mathbf{r}) \sum_{k=1}^{K} \left( s_{n,k} \epsilon^{(0,n,k)}_{\alpha\beta} + \epsilon^{(0,n,0)}_{\alpha\beta} \right) \\ &= \sum_{n,k} s_{n,k} \epsilon^{(0,n,k)}_{\alpha\beta}(\mathbf{r}) + \sum_{n} \epsilon^{(0,n,0)}_{\alpha\beta}(\mathbf{r}), \end{aligned} \tag{4}$$

where $s_{n,k} = \pm 1$ are the spin values to distinguish the different variants. We consider here a generalized case to describe more than two variants, therefore extending the previous simplification in Ref. [5] with only two variants with opposite

eigenstrain. Therefore, an additional summation over $K$ spins per grain is needed, to encode up to $2^K$ different variants, see also [6]. (We note that running roman indices like $k$ enumerate spins and variants, which have to be distinguished from reciprocal lattice vectors $\mathbf{k}$, which are displayed in bold, with components $k_\alpha$. Greek letters are used for spatial components.) In many situations it is beneficial to consider also an offset $\epsilon^{(0,n,0)}_{\alpha\beta}$, as will be illustrated below in Sec. III B. We note that the eigenstrain contributions can differ from grain to grain, to capture different phases or grain orientations. From the spatially constant eigenstrain contributions within each grain in the first line of Eq. (4), in the second line a shorter notation is defined using position dependent eigenstrain contributions, which have a nonvanishing value only inside one grain.

Similarly, we write for the Fourier transformation of $\epsilon^{(0)}_{\alpha\beta}(\mathbf{r})$

$$\hat{\epsilon}^{(0)}_{\alpha\beta}(\mathbf{k}) = \sum_{n,k} s_{n,k}\hat{\epsilon}^{(0,n,k)}_{\alpha\beta}(\mathbf{k}) + \sum_{n} \hat{\epsilon}^{(0,n,0)}_{\alpha\beta}(\mathbf{k}). \tag{5}$$

Consequently, the eigenstress field $\sigma^{(0)}_{\alpha\beta}(\mathbf{r})$ [see Eq. (A15)] has in reciprocal space the form

$$\begin{aligned}\hat{\sigma}^{(0)}_{\alpha\beta}(\mathbf{k}) &= \lambda\delta_{\alpha\beta}\hat{\epsilon}^{(0)}_{\gamma\gamma}(\mathbf{k}) + 2\mu\hat{\epsilon}^{(0)}_{\alpha\beta}(\mathbf{k}) \\ &= \sum_{n,k} s_{n,k}\hat{\sigma}^{(0,n,k)}_{\alpha\beta}(\mathbf{k}) + \sum_{n}\hat{\sigma}^{(0,n,0)}_{\alpha\beta}(\mathbf{k}).\end{aligned} \tag{6}$$

By insertion into the energy expression (2) we obtain the Ising formulation, which is necessary for the quantum annealer. We use here the fixed strain case (ii) with the knowledge that it differs from the free stress case (i) only by the $\mathbf{k} = 0$ terms. Therefore, we need to bring the energy to the form

$$E_{\mathrm{el}} = E_0 + \sum_{i<j} J_{ij}s_i s_j + \sum_i h_i s_i, \tag{7}$$

where $i$ and $j$ are a shorthand notation for the combined grain and variant index, e.g., $i = (n, k)$. With this we get the final elastic energy expression

$$\begin{aligned}E_{\mathrm{el}} = \frac{V}{2}\Bigg\{ &\sum_{\mathbf{k}\neq 0}\sum_{n,m}\left(\hat{\sigma}^{(0,n,0)*}_{\alpha\beta}(\mathbf{k})\hat{\epsilon}^{(0,m,0)}_{\alpha\beta}(\mathbf{k}) - k_\alpha G_{\gamma\beta}k_\delta\hat{\sigma}^{(0,n,0)}_{\alpha\gamma}(\mathbf{k})\hat{\sigma}^{(0,m,0)*}_{\beta\delta}(\mathbf{k})\right) + \lambda\left(\bar{\epsilon}_{\alpha\alpha} - \sum_n \hat{\epsilon}^{(0,n,0)}_{\alpha\alpha}(\mathbf{k}=0)\right)^2 \\ &+ 2\mu\left(\bar{\epsilon}_{\alpha\beta} - \sum_n \hat{\epsilon}^{(0,n,0)}_{\alpha\beta}(\mathbf{k}=0)\right)^2 + \sum_{\mathbf{k}\neq 0}\sum_{n,k}\sum_{m,v}\Big[\hat{\sigma}^{(0,n,k)*}_{\alpha\beta}(\mathbf{k})\hat{\epsilon}^{(0,m,v)}_{\alpha\beta}(\mathbf{k}) - k_\alpha G_{\gamma\beta}k_\delta\hat{\sigma}^{(0,n,k)}_{\alpha\gamma}(\mathbf{k})\hat{\sigma}^{(0,m,v)*}_{\beta\delta}(\mathbf{k}) \\ &+ \lambda\hat{\epsilon}^{(0,n,k)}_{\alpha\alpha}(\mathbf{k}=0)\hat{\epsilon}^{(0,m,v)}_{\alpha\alpha}(\mathbf{k}=0) + 2\mu\hat{\epsilon}^{(0,n,k)}_{\alpha\beta}(\mathbf{k}=0)\hat{\epsilon}^{(0,m,v)}_{\alpha\beta}(\mathbf{k}=0)\Big]s_{n,k}s_{m,v} \\ &+ \sum_{\mathbf{k}\neq 0}\sum_{n,k}\sum_{m}\Big[\hat{\sigma}^{(0,n,k)*}_{\alpha\beta}(\mathbf{k})\hat{\epsilon}^{(0,m,0)}_{\alpha\beta}(\mathbf{k}) + \hat{\sigma}^{(0,m,0)*}_{\alpha\beta}(\mathbf{k})\hat{\epsilon}^{(0,n,k)}_{\alpha\beta}(\mathbf{k}) - k_\alpha G_{\gamma\beta}k_\delta\left(\hat{\sigma}^{(0,n,k)}_{\alpha\gamma}(\mathbf{k})\hat{\sigma}^{(0,m,0)*}_{\beta\delta}(\mathbf{k}) + \hat{\sigma}^{(0,m,0)}_{\alpha\gamma}(\mathbf{k})\hat{\sigma}^{(0,n,k)*}_{\beta\delta}(\mathbf{k})\right) \\ &+ 2\lambda\left(\hat{\epsilon}^{(0,n,k)}_{\alpha\alpha}(\mathbf{k}=0)\hat{\epsilon}^{(0,m,0)}_{\beta\beta}(\mathbf{k}=0) - \bar{\epsilon}_{\alpha\alpha}\hat{\epsilon}^{(0,n,k)}_{\beta\beta}(\mathbf{k}=0)\right) + 4\mu\left(\hat{\epsilon}^{(0,n,k)}_{\alpha\beta}(\mathbf{k}=0)\hat{\epsilon}^{(0,m,0)}_{\alpha\beta}(\mathbf{k}=0) - \bar{\epsilon}_{\alpha\beta}\hat{\epsilon}^{(0,n,k)}_{\alpha\beta}(\mathbf{k}=0)\right)\Big]s_{n,k}\Bigg\},\end{aligned} \tag{8}$$

where $\bar{\epsilon}_{\alpha\beta}$ is the given mean strain. This expression shows explicitly that the elastic energy in a given microstructure with homogeneous elasticity and coherent interfaces between grains, variants or phases leads to an Ising representation, and the values of the coefficients in Eq. (7) can be directly determined.

### C. Description of the underlying workflow

As explained above, we describe the material of interest to be decomposed into "grains", where each of them is entirely in one of the "martensite" states, hence we can describe the entire microstructure through a set of spin variables $\{s_i\}$. We emphasize that the notation as grains does not necessarily require them to be physical grains, but can also be considered as numerical "discretization" unit and also different phases instead of martensite variants can be considered. A simple discretization in this sense is to use little equilateral cuboidal elements, as illustrated for two dimensions in Fig. 1. However, also more complex discretizations are possible and will be discussed in the following. In either way, the elastic energy reduces to combinations of pairwaise interactions between all grains, which follows from the Fourier representation (8) above, which contains only terms up quadratic order in the spin variables $s_i$; see also Ref. [49]. For the cuboidal discretization in the system with periodic boundary conditions, the advantage is that for both the linear and quadratic Ising coefficients in the representation (7) translation invariance can be employed. This reduces the computational effort drastically, as only one "self energy" for an arbitrary grain has to be computed, as well as the "interaction energy" of one grain with all other grains. For all other grains, one obviously gets the same values. The result of such a calculation is illustrated as heat map in Fig. 2, where the color coding shows the strength of the interaction, i.e., the magnitude of the Ising coefficients $J_{ij}$ for two grains enumerated by $i$ and $j$. Here, one of the grains is placed in the center of the system, and the interaction energy with all grains is shown. Therefore, the computational effort for calculating the Ising coefficients scales as $N$, where $N$ is the number of cuboidal grains. This figure shows that besides the translational invariance, also discrete symmetries may be employed, depending on the type of transformation strain.

In contrast, an irregular discretization as in Fig. 3 requires the computation of all interaction energies between all pairs of grains, hence we have a scaling of the effort as $N^2$. Such a

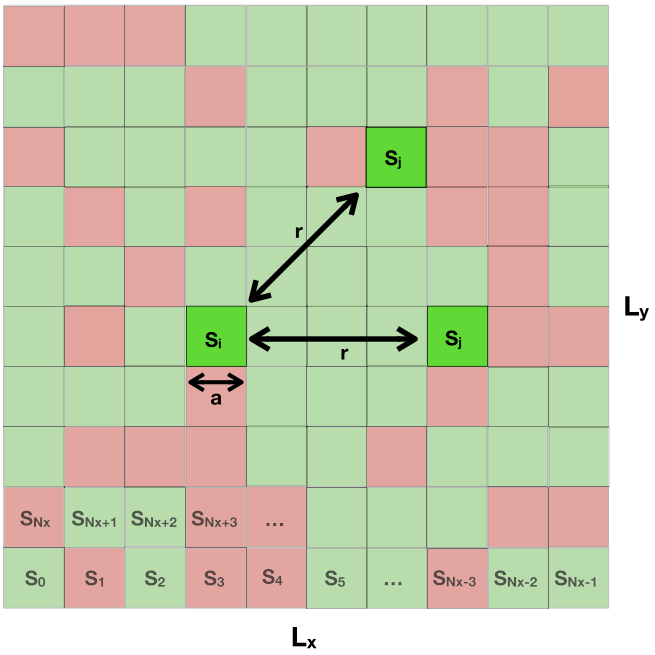


FIG. 1. Two-dimensional discretization of the system using cuboidal "grains."

microstructure could, e.g., be imported from an EBSD mapping of a material of interest. To mimic a realistic microstructure, also a Voronoi tesselation can be used. Here, we use the open source software library voro++ for this purpose [50,51]. We mention in passing that although we use isotropic elasticity, still the eigenstrain can depend on grain orientation. Therefore, we can assign a (random) orientation to each grain in the stage of the Voronoi tesselation, which can then be used for a tensor rotation of the eigenstrain.

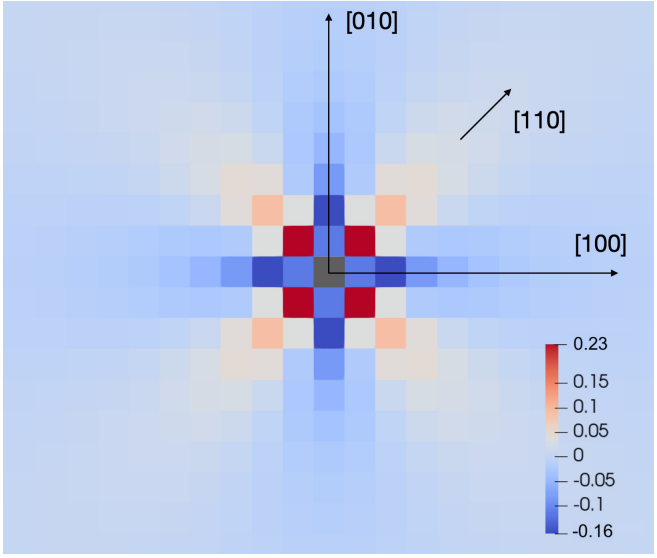


FIG. 2. Each grain can be in the states $s_i = \pm 1$. Interaction energies of two grains of equal variant type ($s_i = s_j$) in the case of a shear eigenstrain, as described by Eq. (14), and vanishing average stress. The interaction energy per length is given in units of $\lambda a^3 \epsilon_0^2$, and the computations were done using a system size of $L_x/a = L_y/a = 50$ with a Poisson ratio of $\nu = 1/4$.

For the computation of the Ising coefficients, the derived formula (8) can be used directly. Alternatively, it can be easier to use the strategy described in Ref. [6]. The idea is that one uses explicit settings of the spins by assigning to them values 0 and 1. Then, it is sufficient to perform calculations with (i) all spins being equal to zero, (ii) one single spin being equal to $\pm 1$, whereas all other vanish, and (iii) for calculation of the interaction energies $J_{ij}$ additionally computations with two nonvanishing spins $s_i = s_j = 1$, whereas all other vanish, are needed, see Refs. [5,6] for details.

Additionally, it makes sense to separate the terms with $\mathbf{k} \neq 0$ from the one with $\mathbf{k} = 0$, as the latter is related to a given external strain. These latter terms can be calculated analytically, which has the advantage that a change of the external boundary conditions does not require a (numerically expensive) recomputation of the Ising coefficients.

After calculation of the Ising coefficients $J_{ij}$ and $h_i$, the problem is ready for implementation on a quantum annealer. Due to the probabilistic nature of the quantum annealing process also higher energy states are found, specially if close low energy states are present. Therefore, a suitable number of repetitions of the process is made and the solution with the lowest detected energy is chosen. In the case that the Ising problems do not match the QPU's architecture, so called chains, i.e., subgraphs of coupled qubits, cover one problem variable through the minor embedding [52,53]. In addition, for large problem sizes hybrid quantum annealing takes additional advantage of combining QPU computations with classical algorithms, allowing for up to 11616 spin variables on the D-Wave Advantage system [52,54,55]. Finally, the resulting spin configuration obtained by the quantum annealing process is visualized according to the generated Voronoi grains.

## III. RESULTS

In this section we discuss several aspects, applications and extensions of the presented method. First, in Sec. III A we show that even systems with a rather high number of grains can be simulated efficiently with quantum annealing. The second example in Sec. III B investigates possible self organization processes in solid electrolytes for battery applications. In Sec. III C we illustrate how apart from volumetric effects also interfacial energy contributions can be included. Finally, in Sec. III D we emphasize the importance of high precision elasticity calculations and the influence of possible real space interaction cutoffs.

### A. Large-scale simulation of equilibrium microstructures

In contrast to microstructure evolution simulation approaches, the present approach aims at determining directly (constrained) equilibrium patterns. Here, the energy can be minimized by properly selecting the variants (or phases) for each grain, depending on the external mechanical load. We show that for quantum annealing simulations with several thousand grains are easily feasible. We note that the total time for determining the ground state configurations for simulations with $N = 2500$ grains, as depicted in Fig. 3, do not

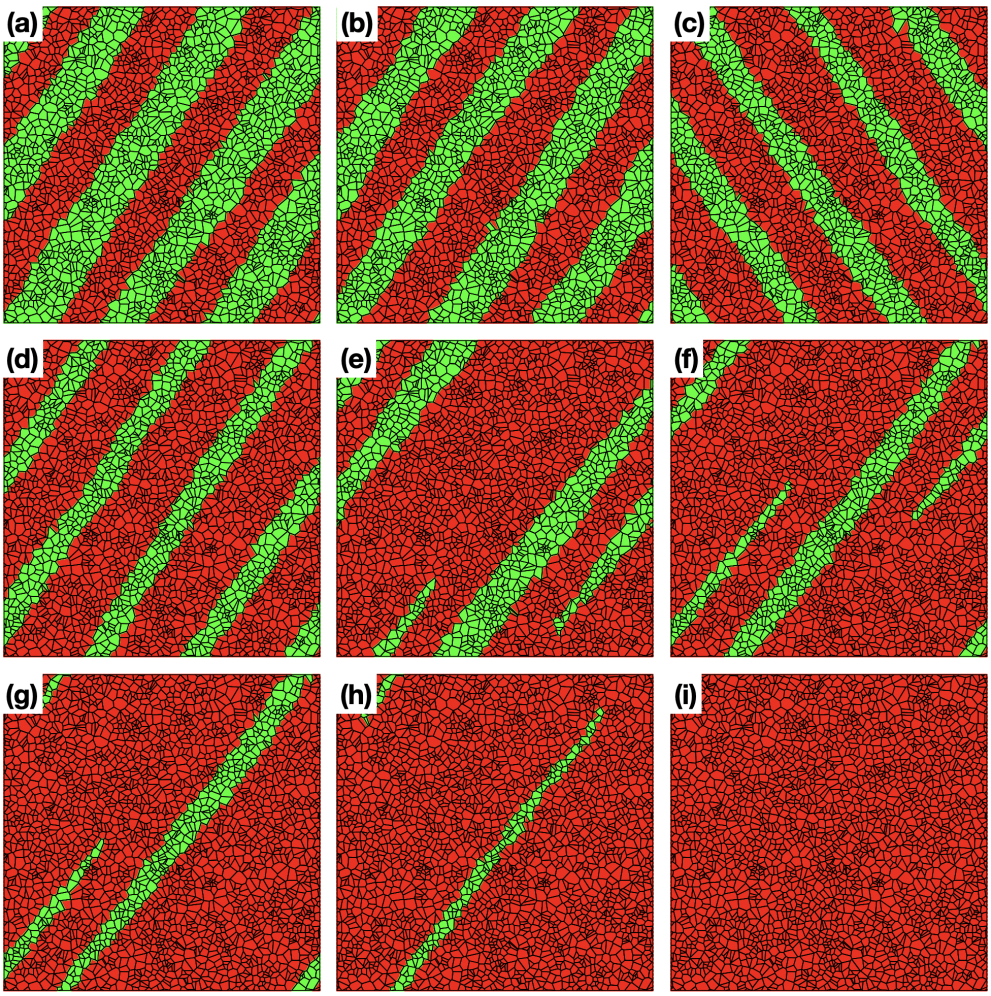


FIG. 3. Equilibrium variant distribution in a microstructure with uniform grain orientation. The microstructures consist of 2500 coherent grains, and a tensile strain is applied in horizontal ($x$) direction. Red (green) grains correspond to variant $s_i = +1$ ($s_i = -1$), as described through the eigenstrain tensor (9). The tensile strain is (a) $\langle\epsilon_{xx}\rangle/\epsilon_0 = 0$, (b) $\langle\epsilon_{xx}\rangle/\epsilon_0 = 0.165$, (c) $\langle\epsilon_{xx}\rangle/\epsilon_0 = 0.495$, (d) $\langle\epsilon_{xx}\rangle/\epsilon_0 = 0.66$, (e) $\langle\epsilon_{xx}\rangle/\epsilon_0 = 0.825$, (f) $\langle\epsilon_{xx}\rangle/\epsilon_0 = 0.99$, (g) $\langle\epsilon_{xx}\rangle/\epsilon_0 = 1.155$, (h) $\langle\epsilon_{xx}\rangle/\epsilon_0 = 1.305$, and (i) $\langle\epsilon_{xx}\rangle/\epsilon_0 = 1.32$. The Poisson ratio is $\nu = 1/4$.

require more than roughly one minute on a D-Wave quantum annealer if a hybrid solver is used (the system is too big for a pure quantum annealer solution); in fact, the pure QPA access time is significantly lower. However, one has to keep in mind that the Ising coefficients need to be precomputed, and this becomes then the computationally expensive part, as $\sim N^2$ interactions need to be calculated with high precision.

In the presented case, we distinguish between two martensite variants, hence one spin variable per grain is required. The eigenstrain is given as

$$\epsilon^{(0)}_{\alpha\beta} = s_i \begin{pmatrix} \epsilon_0 & 0 & 0 \\ 0 & -\epsilon_0 & 0 \\ 0 & 0 & \epsilon_0 \end{pmatrix} \tag{9}$$

in each grain, relative to the austenitic phase, without consideration of a grain rotation. The strength of the transformation is controlled by the parameter $\epsilon_0$, and additionally a varying tensile strain is applied in lateral ($x$) direction. Figure 3 shows the resulting variant distribution of equally orientated grains for different strain strengths. For a vanishing tensile strain, stripe patterns arise, which are discussed in more detail in Ref. [5]. For increasing strain, the stripes are getting thinner, until they are not connecting anymore. A criticial strain of about $\langle\epsilon_{xx}\rangle/\epsilon_0 \approx 1.32$ [see panel (i)] leads to a uniform microstructure, i.e., only red grains with $s_i = +1$ remain.

The result shows that even with a straightforward generalization to 3D structures it is possible to have sufficiently large number of grains in each spatial direction, and therefore the approach is well suited to generate strain dependent microstructures for representative volume elements.

### B. Solid electrolyte $Li_7La_3Zr_2O_{12}$ (LLZO)

$Li_7La_3Zr_2O_{12}$ (LLZO) is a promising ceramic material which can be used as electrolyte in all-solid-state batteries. It has a high-ionic conductivity and can be used with lithium as anode material, hence allowing for a high-energy density and stability against failure. However, the room temperature equilibrium phase of LLZO is a tetragonal phase, which has a much lower Li ion conductivity than the metastable cubic phase. The latter can be stabilized by alloying, e.g., with Ta at increased costs. Therefore, it is desirable to perform such dopings only to a minimum amount. From a thermodynamic perspective, the doping level determines the phase fractions of

the cubic and tetragonal phases, but does not make predictions for their spatial alignment, as the (bulk) chemistry depends only on the overall volume fractions but not the arrangement.

In this section we aim to investigate to which extent elastic effects, which arise due to the misfit between tetragonal and cubic grains, can affect their equilibrium arrangement by minimization of the elastic energy. This may in the future enable a "grain engineering" by enabling a self-organization process, if "channels" of the cubic phase inside a tetragonal matrix could lead to increased ionic conductivity through percolation. To stay in the framework of the presented theoretical approach, we make a number of simplifying assumptions to keep the description simple and to rather sketch a possible way for future optimized electrolyte fabrication. In detail, the assumptions are: (i) We assume all grains to be equally oriented. (ii) The grains are coherently connected and we use the same (isotropic) elastic constants for both phases. (iii) We consider for simplicity apart from the cubic phase (spin $-1$) only one tetragonal variant (spin $+1$). (iv) The description is two-dimensional with a plane strain setup.

Points (i) and (ii) are probably the most serious restrictions of the current description, and therefore we expect the predictions to be rather qualitative and setting an upper bound to the possible influence of elastic effects. The assumptions (iii) and (iv) are only technical simplifications, and a generalization to a full three-dimensional description with more variants is in the spirit of the general approach described above and mainly increases the computational effort.

Concerning the description of the mechanical properties of LLZO, we refer to the previous work [47,48,56]. The lattice parameters for tetragonal LLZO, which is stable at ambient temperature, are given as $a_{\mathrm{tet}} = 13.1846$ Å and $c_{\mathrm{tet}} = 12.6390$ Å. In the desired cubic case the lattice parameter is given as $a_{\mathrm{cub}} = 13.03286$ Å. We employ the previous definition of the eigenstrain [Eq. (4)] with two variants, $K = 1$, and $N$ grains. Then, the resulting eigenstrain reads

$$\epsilon^{(0)}_{\alpha\beta}(\mathbf{r}) = \sum_{n}^{N} \theta_n(\mathbf{r})\left(s_1^{(n)}\epsilon^{(0,n,1)}_{\alpha\beta} + \epsilon^{(0,n,0)}_{\alpha\beta}\right), \tag{10}$$

with eigenstrain tensor components $\epsilon^{(0,n,1)}_{\alpha\beta}$ and constant eigenstrain offset $\epsilon^{(0,n,0)}_{\alpha\beta}$. We use the cubic phase ($s = -1$) as reference state, hence $\epsilon^{(0)}_{\alpha\beta} = 0$ in such a grain, whereas in a tetragonal grain we have

$$\epsilon^{(0)}_{\alpha\beta} = \begin{pmatrix} \frac{a_{\mathrm{tet}}-a_{\mathrm{cub}}}{a_{\mathrm{cub}}} & 0 & 0 \\ 0 & \frac{c_{\mathrm{tet}}-a_{\mathrm{cub}}}{a_{\mathrm{cub}}} & 0 \\ 0 & 0 & \frac{a_{\mathrm{tet}}-a_{\mathrm{cub}}}{a_{\mathrm{cub}}} \end{pmatrix} = \begin{pmatrix} 0.011643 & 0 & 0 \\ 0 & -0.030221 & 0 \\ 0 & 0 & 0.011643 \end{pmatrix}. \tag{11}$$

These relations allow to uniquely determine $\epsilon^{(0,n,1)}_{\alpha\beta}$ and $\epsilon^{(0,n,0)}_{\alpha\beta}$. The elastic properties are—in isotropic approximation—described to good accuracy with a Poisson ratio $\nu = 1/4$ as before.

Besides the mechanical component, which is responsible for the spatial arrangement of the phases, also a chemical component is important, as it fixes the volume fraction of the phases. Such a perspective is based on the picture that the chemical energy is higher than the elastic energy. However, in general also chemomechanical couplings can play a role if both energy contributions are of a comparable order of magnitude. In this case, it is also possible that strong mechanical misfits affect the phase fractions, as a reduction of the elastic energy can be stronger than a deviation from the equilibrium partitioning from a purely chemical perspective. To qualitatively study such transitions, we add a description of the chemical contribution to the free energy and treat the coefficients in this energy term as adjustable parameters.

To lowest order, a deviation of the chemical free energy from a situation with equilibrium phase fractions is quadratic in the volume fraction deviation. Hence, this energy contribution can be written as

$$\Delta E = V\gamma\left(\sum_{i=1}^{N} f_i s_i - f\right)^2 = 2V\gamma\sum_{i<j}^{N} f_i f_j s_i s_j - 2V\gamma f\sum_{i}^{N} f_i s_i + \text{const.} \tag{12}$$

Here, $f$ is a parameter quantifying the expected equilibrium volume fraction of the two phases, which is controlled by the alloying, as described above. It ranges between $-1$ for a purely cubic and $+1$ for a tetragonal system. Therefore, in particular $f = 0$ corresponds to equal volume fractions of the two phases. The parameter $f_i$ is the volume fraction of grain $i$, hence $\sum_i^N f_i = 1$ holds. Finally, $\gamma$ controls the strength of the chemical energy contribution. It relates the curvature of the composition dependent chemical free energy curves to the elastic contribution, and can therefore be used to tune between a chemically and a mechanically dominated system. As the chemical energy expression (12) is quadratic in the spin variable $s_i$, it can directly be implemented on the quantum annealer, together with the elastic contribution. The quantum annealing calculations are then performed via hybrid computations, which allow to reliably find the ground state even for larger systems.

Figure 4 shows the resulting equilibrium variant distribution. In all panels the same Voronoi tesselated microstructure with 100 grains is used. Furthermore, all grains have the same orientation, hence the same eigenstrain (11) is used for all of them. As mechanical boundary conditions we use vanishing average strain, $\langle\epsilon_{\alpha\beta}\rangle = 0$. In horizontal direction the weighting parameter $\gamma$ and in vertical direction phase fraction parameter $f$ is varied. Here, green (red) grains correspond to the cubic (tetragonal) phase. The patterns in Figs. 4(a)– 4(d) consist only of the cubic grains due the choice $f = -1$ in the chemical energy. We note that in this state the system is stress free due to the chosen mechanical boundary condition $\langle\epsilon_{\alpha\beta}\rangle = 0$. All pictures in the right column [Figs. 4(d), 4(h), 4(l), and 4(p)] correspond to $\gamma = 0$, which means that the chemical energy contribution is absent. As then the energy consists only of the elastic contribution, the system becomes completely cubic in this case due to the chosen reference of vanishing eigenstrain in the cubic phase. In contrast, the

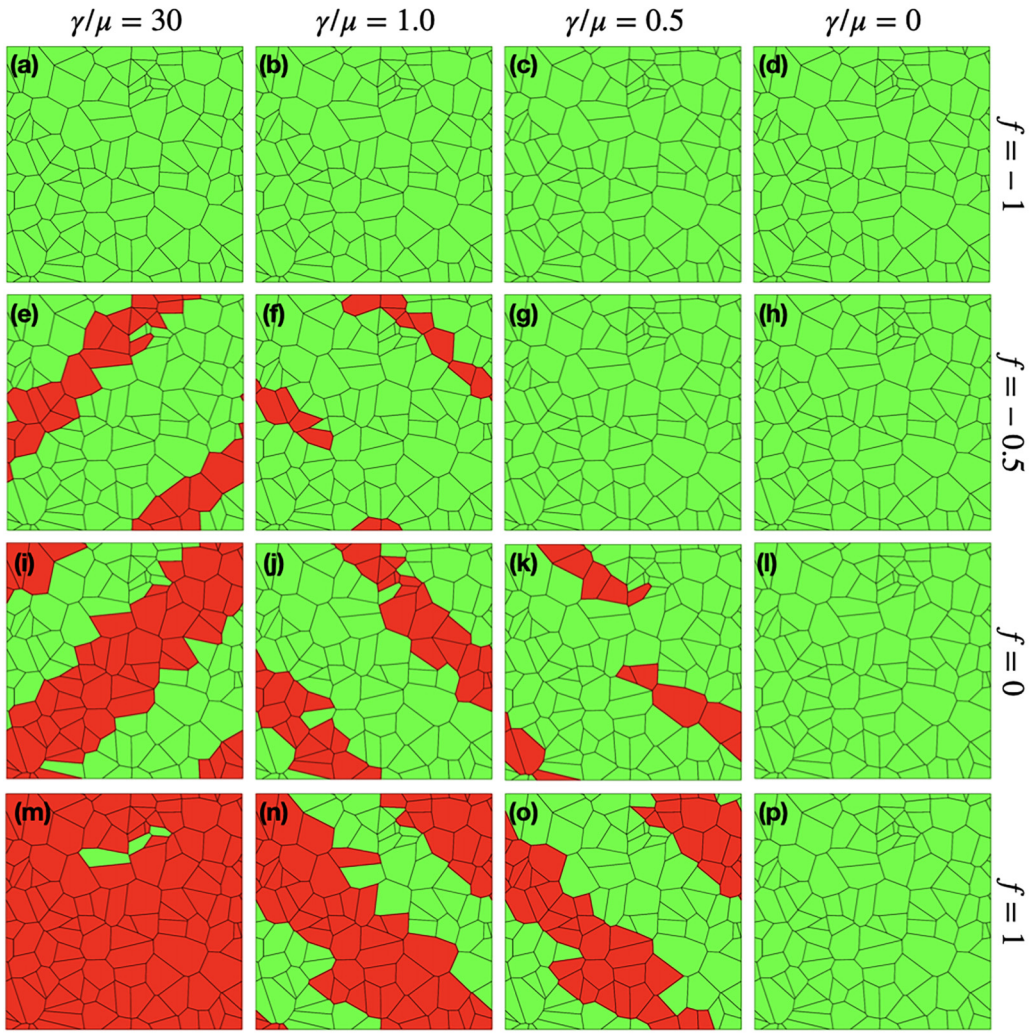


FIG. 4. Equilibrium phase distribution of tetragonal and cubic phases in LLZO for grains with uniform orientation. The microstructures consist of 100 grains and the parameters $\gamma$ and $f$ are varied. Red grains correspond to $s_i = +1$, i.e., the tetragonal phase, green to $s_i = -1$, which is the cubic phase.

chemical energy dominates for the cases in the left column [Figs. 4(a), 4(e), 4(i), and 4(m)], and then the volume fractions are close to the expected value $f$ from the chemical perspective. Nevertheless, the elastic contribution is still sufficient to favor an ordering as inclined stripes similar to the above situation in Fig. 3, with an orientation as expected from the analysis in Ref. [5]. Also, a small cubic island remains even in the case $f = 1$ in Figs. 4(m). In the bottom row, the chemical contribution favors purely tetragonal systems ($f = 1$), whereas the elastic energy favors the cubic state due the the mechanical boundary conditions. In this extreme case the volume fractions are then strongly controlled by the weighting parameter $\gamma/\mu$. For intermediate values, where two-phase structures are found, the strip patterns are are more rugged in comparison to the patterns in Fig. 3, which is mainly due to the smaller number of grains. For all other cases, as, e.g., for the row $f = 0$, where from a chemical perspective equal volume fractions of the phases are expected, the overall energy minimization including elastic contributions lead to deviations from this expectation, hence highlighting the aforementioned strong chemomechanical coupling.

As a consequence we observe indeed a tendency for the formation of ion conducting channels through the presence of elastic effects for suitable mechanical boundary conditions. However, it has to be pronounced that here all grains are assumed to have the same orientation, and therefore also the tetragonal distortion leads to an expansion in both $x$ and $z$ direction. As long as the orientation remains in this plane by a grain rotation, the eigenstrain tensor (11) remains invariant, hence favoring such a self-organization process toward an increased ionic conductivity of the solid electrolyte.

### C. Interfacial energy

So far, we have considered with the elastic and chemical contributions only bulk energies. As a consequence, there is no selection of a length scale. In other words, a rescaling of the pattern (including a change of the grain size) will lead to identical patterns, and only the total energy changes according to its proportionality to the system volume.

The inclusion of interfacial contributions therefore leads to new physical effects, as—depending on the length scale—the

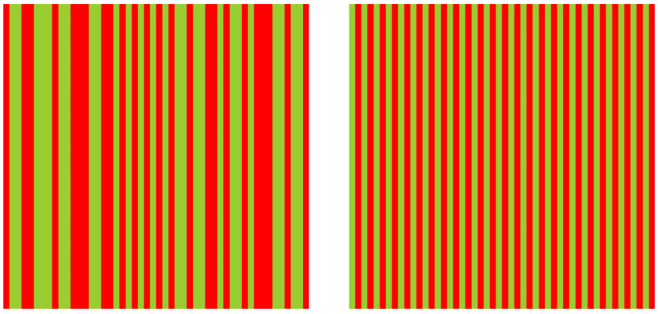

FIG. 5. Equilibrated microstructures for zero average strain and shear transformations with vanishing and negative interfacial energy in a system of $50 \times 50$ cuboidal grains. Left: $\sigma/\mu\epsilon_0^2 a = 0$, right: $\sigma/\mu\epsilon_0^2 a = -1$. The length is measured in multiples of the lattice unit $a$, the Poisson ratio is $\nu = 1/4$.

bulk and interface energies can compete. In fact, with the interfacial energy density (per area) $\sigma$, the ratio $\sigma/\mu$ sets a characteristic length scale. For a positive value of $\sigma$ we expect a coarsening tendency of the microstructure, and hence in equilibrium the amount of interfaces shall be minimized in particular if the interfacial energy dominates.

To formulate an interfacial energy (per unit length in 2D) in the spirit of an Ising model for the quantum annealer, we use a nearest-neighbor interaction, which penalizes interfaces between different variants, using

$$E_{\text{interface}} = \frac{1}{2} \sum_{i,j(\text{NN})} a_{ij} \tilde{\sigma}_{ij} (1 - s_i s_j), \tag{13}$$

where $a_{ij}$ is the interface length between grain $i$ and $j$ and $\tilde{\sigma}_{ij}$ is the interfacial energy for this pairs of grains. The formulation (13) is for general anisotropic interface energies, and for demonstrational purposes we focus here on the isotropic case with $\tilde{\sigma}_{ij} \equiv \sigma$ for all interfaces. The summation in this formula is limited to nearest-neighbor (NN) pairs, but also generalizations to longer ranged interactions are conceivable to mimic additional interactions.

As a simple illustration we use first the case of a shear transformation with eigenstrain

$$\epsilon^{(0)}_{\alpha\beta} = s_i \begin{pmatrix} 0 & \epsilon_0 & 0 \\ \epsilon_0 & 0 & 0 \\ 0 & 0 & 0 \end{pmatrix}, \tag{14}$$

which was conceptually discussed from point of view of elastic effects in Ref. [5]. If we use a discretization by equally sized cubes (hence, all $a_{ij} = a$) without interfacial effects, $\sigma = 0$, then the equilibrium pattern for fixed and vanishing average strain boundary conditions, $\langle \epsilon_{\alpha\beta} \rangle = 0$, are horizontal or vertical stripes with equal volume fractions of the two variants, hence the microstructure is effectively one-dimensional. In this case, the entire pattern is stress free, as in each lamella $\epsilon_{\alpha\beta} = \epsilon^{(0)}_{\alpha\beta}$. Consequently, an arbitrary arrangement of stripes with equal amounts of the red and green phases minimizes the elastic energy to zero; see left panel of Fig. 5. Consequently, the selection among all the possible stripe patterns becomes entirely through the interfacial energy for $\sigma \neq 0$. Thus, for $\sigma > 0$ the system minimizes the total energy by having a stripe pattern with as few interfaces as possible. With the condition $\langle \epsilon_{\alpha\beta} \rangle = 0$ we therefore obtain two equally sized red and green stripes, provided that the interfacial energy is not too high that even a strained single phase pattern is favorable. In turn, for a negative interfacial energy $\sigma < 0$ the optimal microstructure consists of a regular array of lamellae with minimum width $a$; see right panel in Fig. 5.

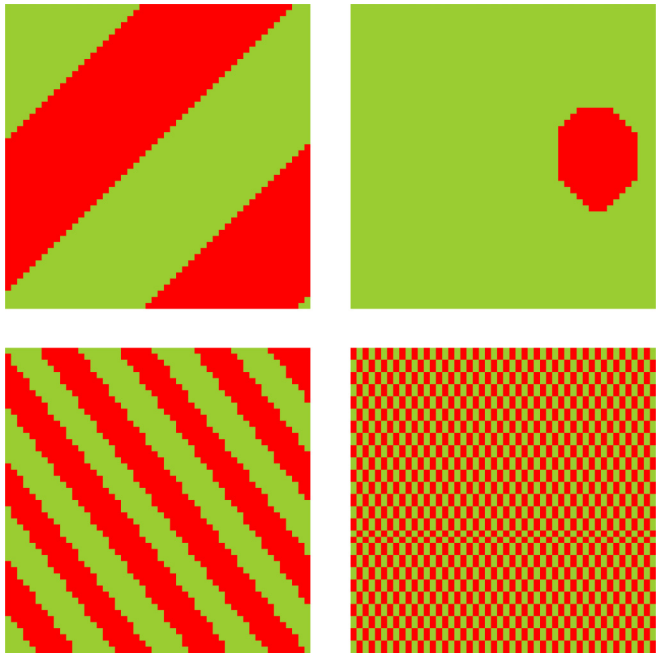

FIG. 6. Top row: Equilibrated microstructures for zero average strain and tetragonal transformations with different values of positive interfacial energy in a system of $50 \times 50$ cuboidal grains. Left: $\sigma/\mu\epsilon_0^2 a = 1$, right: $\sigma/\mu\epsilon_0^2 a = 9$. Bottom row: The same for negative interfacial energy: Left: $\sigma/\mu\epsilon_0^2 a = -0.06$, right: $\sigma/\mu\epsilon_0^2 a = -0.07$. The length is measured in multiples of the lattice unit $a$, the Poisson ratio is $\nu = 1/4$.

For a tetragonal eigenstrain, see Eq. (9), patterns with regular inclined stripes for $\langle \epsilon_{\alpha\beta} \rangle = 0$ similar to Figs. 3 and 4 appear without interfacial energy. For a positive interfacial energy $\sigma > 0$, an increasing value of $\sigma$ first leads to a reduction of the number of stripes as well as a rotation of the stripes to comply with the periodic boundary conditions (see top row of Fig. 6). A higher value of the interfacial energy destroys this morphology and leads to patterns with unequal amounts of the variants, as the interfacial energy overweights the elastic effects, though the latter alone would favor configurations where the mean eigenstrain vanishes due to the boundary condition. In a narrow intermediate parameter range, the appearing pattern contains a nucleus of one variant inside a matrix of the other one (see top right panel of Fig. 6). The elastic energy stabilizes the nucleus for the same argument as just above, whereas the interfacial energy balances this contribution and favors the disappearance of the nucleus. For even higher values of $\sigma$ the system becomes single phased due to the dominance of the interfacial energy. For negative interfacial energy, patterns with more interfaces become favorable (see bottom row of Fig. 6). Initially, this leads to an increase of the stripe density and change of the orientation angle with decreasing interfacial energy, which

then start to become unstable up to the point where the lamellar microstructure is entirely destroyed. This transition occurs within a very narrow range of interfacial energies.

### D. Discussion on the elastic energy calculation

The key element of the quantum-annealer-based determination of the elastic ground state microstructure is the formulation via pairwise interactions in the Ising formulation. An example for the interaction coefficients $J_{ij}$ is shown in Fig. 2. This heatmap shows that the interactions with the closest neighbors is highest and decays with the distance between the grains. Depending on the dimension of the system, the elastic interactions decay asymptotically either as $1/r^2$ in 2 dimensions or $1/r^3$ in 3D. There are similarities to the computations of long ranged Coulomb interactions, e.g., for molecular dynamics simulations, which require the use of Ewald summation techniques to properly capture the long range tails of the interactions in periodic systems. Therefore, also here the use of a real space cutoff for the elastic grain-grain interactions is critical, although the interactions seem to decay quickly.

To emphasize this effect, we consider again the shear transformation case (14), which leads to stripe patterns; see Fig. 5. As mentioned before, this example can be solved analytically easily, as having a vanishing stress in each stripe by $\epsilon_{\alpha\beta} = \epsilon^{(0)}_{\alpha\beta}$ leads to a completely stress free case, which is compatible with both the boundary conditions $\langle\sigma_{\alpha\beta}\rangle = 0$ and $\langle\epsilon_{\alpha\beta}\rangle = 0$, provided that the volume fractions of the two variants is equal. However, from the picture of pairwise interactions in the Ising representation this solution is not obvious. As all the Ising coefficients are different from zero, it is an almost miraculous cancellation of all $N(N-1)/2$ mutual interactions, such that the total elastic energy is exactly zero (apart from a constant offset, which is typically not considered for the annealer formulation). If now the range of the interactions is artificially cut off, then it cannot be expected that the elastic energy agrees with the analytical calculation.

To illustrate this effect, we set up a regular stripe microstructure manually in a system discretized by $50 \times 50$ cuboidal grains with a given lamella thickness $\lambda$. Additionally, we impose an artificial cutoff to the range of the interactions by setting $J_{ij} = 0$ beyond a given separation of the considered grains. Figure 7 shows the resulting elastic energy, as computed from the truncated Ising summation for different stripe thicknesses $\lambda$. In all cases we see that the expected energy $E = 0$ is only reached without a cutoff (in the periodic system, this is achieved if the range of the interaction is taken at least half the system length, which is 25 in the example). With the cutoff, the energy is obtained incorrectly, and then also the quantum annealer is obviously not able to find the physically correct ground state configuration. Qualitatively, the energy is close to the expected value, if the cutoff range is significantly larger than the stripe thickness $\lambda$, but as in general the equilibrium microstructure can only be obtained based on exact Ising coefficients, we can therefore conclude that the use of any cutoff for the elastic interaction energy calculation is not appropriate.

Apart from the issue of a real space cutoff, also possible numerical rounding errors have to be considered. As the elastic energy is represented through a summation over $\sim N^2$ terms, even small errors can lead in total to improper results. For the shear transformation example, the grain-grain interaction at a distance of 20 lattice units in [100] direction has decayed to about 2% of the maximum interaction strength at next-to-nearest-neighbor interactions (see Fig. 2). To illustrate the potential influence of numerical inaccuracies, a random noise of this strength is added artificially to all considered pair interaction coefficients, leading to modified total energies, which do not converge to the analytical result without cutoff anymore; see Fig. 7. Therefore, the comparison to an analytically known solution like the stripe patterns can help to identify possible rounding errors.

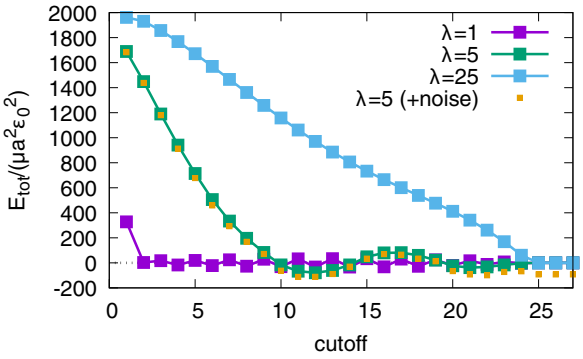


FIG. 7. Total elastic energy as expressed through the Ising summation for a regular lamellar structure with strip width $\lambda$ as function of the real space interaction cutoff. The correct elastic energy $E_{\text{tot}} = 0$ is reached only without cutoff, i.e., larger than half of the system size, which is 25 here. For the case with noise, an uncorrelated random variable with uniform distribution, vanishing mean value and maximum magnitude of 2% of the strongest grain-grain interaction in [100] interactions is added to all interaction parameters $J_{ij}$ up to the cutoff distance, leading to an inappropriate total energy even without cutoff.

In many cases, the ground state configuration is unique, but for example for the shear transformation with the irregular "barcode" patterns as in Fig. 5, the ground state is strongly degenerate. Therefore, the Ising coefficients need to computed with very high accuracy in order not to introduce spurious biases. We indeed obtain for high resolution Fourier transformation computed interaction coefficients always different patterns by the quantum annealer, which is an indication for proper representation of the elastic energy through the Ising summation. In essence, a precise calculation of the interaction energy is therefore essential, and rough estimated, e.g., based on the proper long distance asymptotics, not sufficient.

## IV. CONCLUSION AND OUTLOOK

The present paper's central result is the extended description and investigation of the underlying elastic calculations of the microstructure optimization via quantum annealing. We describe the underlying calculations of long-ranged elastic interactions in reciprocal space and show the resulting direct Ising formulation for the quantum annealer. Large scale simulations of equilibrium microstructures with 2500 grains and varying tensile strain result in the expected stripe

patterns, which are getting thinner for increasing strain. Here, the quantum annealing part requires just roughly one minute of computing time and presents no drastically increase with increasing system sizes. This shows that also a generalization to 3D structures with huge system sizes and therefore the generation of microstructures with representative volume elements is possible.

The application of the quantum annealing microstructure equilibration to the solid electrolyte LLZO includes a chemical energy component, which competes with the elastic energy and influences the resulting microstructures. In essence, the elastic effects favor a formation of ion conducting channels through a self-organization process for suitable mechanical boundary conditions. We note that these findings are based on a number of simplifying assumptions, but future investigations may extend the model's complexity toward an optimization of solid electrolytes. Therefore, this application is a promising step toward quantum-computing-based material design.

Further extensions include interfacial contributions to investigate the competition between bulk and interface energies and their influence on the microstructure formation.

The truncation of the elastic interaction range through a real space cutoff is tempting, however, we show that this is not useful due to an artificial scale selection, which results in improper microstructure predictions. Therefore, all interactions between the grains have to be taken into account with high accuracy. Fortunately, this is possible on the quantum annealer without great losses in computing time also for large system sizes.

## ACKNOWLEDGMENTS

This work was funded by the German Federal Ministry of Education and Research (BMBF) via the project ALANO (Grant No. 13XP0396B) and the Helmholtz project ZeDaBase. Open access was funded by the Deutsche Forschungsgemeinschaft (DFG, German Research Foundation) Grant No. 491111487. The authors gratefully acknowledge the Jülich Supercomputing Centre [57] for funding this project by providing computing time on the D-Wave Advantage System JUPSI through the Jülich UNified Infrastructure for Quantum computing (JUNIQ).

## APPENDIX: DERIVATION OF THE ELASTIC ENERGY

In this Appendix we determine the elastic equilibrium state for a given eigenstrain distribution and express the elastic energy for this equilibrated state in reciprocal space.

Generally, the Fourier transformation of a (real) function $f(\mathbf{r})$ is denoted as

$$\hat{f} = \frac{1}{V}\int_V f(\mathbf{r})\exp(i\mathbf{kr})\,d\mathbf{r}, \tag{A1}$$

inside a periodic cuboidal system with volume $V = L_x \times L_y \times L_z$. Then, the back transformation reads

$$f(\mathbf{r}) = \sum_{\mathbf{k}} \hat{f}(\mathbf{k})\exp(-i\mathbf{kr}), \tag{A2}$$

using the reciprocal lattice vectors

$$\mathbf{k} = 2\pi\left(\frac{n_x}{L_x}, \frac{n_y}{L_y}, \frac{n_z}{L_z}\right), \quad n_i \in \mathbb{Z}. \tag{A3}$$

The orthogonality between the base functions is expressed through Parseval's theorem, which holds for arbitrary functions $f_1(\mathbf{r})$, $f_2(\mathbf{r})$ and their Fourier transforms $\hat{f}_1(\mathbf{k})$, $\hat{f}_2(\mathbf{k})$,

$$\frac{1}{V}\int_V f_1(\mathbf{r})f_2(\mathbf{r})\,d\mathbf{r} = \sum_{\mathbf{k}} \hat{f}_1(\mathbf{k})\hat{f}_2^*(\mathbf{k}), \tag{A4}$$

where the star denotes complex conjugation. For numerical implementations, Fast Fourier libraries like FFTW can be used [58].

The strain can be split into a homogeneous (macroscopic shape deformation) and heterogeneous part [59]

$$\epsilon_{\alpha\beta}(\mathbf{r}) = \bar{\epsilon}_{\alpha\beta} + \delta\epsilon_{\alpha\beta}(\mathbf{r}). \tag{A5}$$

The homogeneous strain $\bar{\epsilon}_{\alpha\beta}$ is then defined such that the mean value of the fluctuation part vanishes,

$$\langle\delta\epsilon_{\alpha\beta}(\mathbf{r})\rangle = \frac{1}{V}\int_V \delta\epsilon_{\alpha\beta}(\mathbf{r})\,dV = 0. \tag{A6}$$

Similarly, we split the elastic energy into a contribution $E_1$ which does not contain the fluctuations $\delta\epsilon_{\alpha\beta}$ and the remaining part $E_2$,

$$E_1 = \int_V \left(\frac{\lambda}{2}\left(\bar{\epsilon}_{\alpha\alpha} - \epsilon^{(0)}_{\alpha\alpha}(\mathbf{r})\right)^2 + \mu\left(\bar{\epsilon}_{\alpha\beta} - \epsilon^{(0)}_{\alpha\beta}(\mathbf{r})\right)^2\right) d\mathbf{r} \tag{A7}$$

and

$$E_2 = \int_V \left(\frac{\lambda}{2}\left(\delta\epsilon^2_{\alpha\alpha}(\mathbf{r}) - 2\epsilon^{(0)}_{\alpha\alpha}(\mathbf{r})\delta\epsilon_{\beta\beta}(\mathbf{r})\right) + \mu\left(\delta\epsilon^2_{\alpha\beta}(\mathbf{r}) - 2\epsilon^{(0)}_{\alpha\beta}(\mathbf{r})\delta\epsilon_{\alpha\beta}(\mathbf{r})\right)\right) d\mathbf{r}, \tag{A8}$$

hence $E_{\mathrm{el}} = E_1 + E_2$.

Elastic equilibrium can be expressed through the minimization of the energy. Since $E_1$ and $E_2$ are functionals of independent degrees of freedom, the minimzation of $E_{\mathrm{el}}$ requires the separate minimization of $E_1$ and $E_2$. Here, we distinguish between two cases, namely (i) vanishing mean stress, $\langle\sigma_{\alpha\beta}\rangle = 0$, and (ii) given average mean strain, $\langle\epsilon_{\alpha\beta}\rangle = \bar{\epsilon}_{\alpha\beta}$.

In case (i) the elastic energy is minimized with respect to the (total) displacement components as degrees of freedom. This includes the minimization of $E_1$ with respect to the homogeneous strain contributions $\bar{\epsilon}_{\alpha\beta}$,

$$\frac{\partial E_1}{\partial\bar{\epsilon}_{\alpha\beta}} = \int_V \left[\lambda\delta_{\alpha\beta}\left(\bar{\epsilon}_{\gamma\gamma} - \epsilon^{(0)}_{\gamma\gamma}(\mathbf{r})\right) + 2\mu\left(\bar{\epsilon}_{\alpha\beta} - \epsilon^{(0)}_{\alpha\beta}(\mathbf{r})\right)\right] d\mathbf{r} = 0. \tag{A9}$$

By definition the mean stress is given in the isotropic case as

$$\bar{\sigma}_{\alpha\beta} = \langle\sigma_{\alpha\beta}(\mathbf{r})\rangle = \lambda\delta_{\alpha\beta}\left(\bar{\epsilon}_{\gamma\gamma} - \left\langle\epsilon^{(0)}_{\gamma\gamma}(\mathbf{r})\right\rangle\right) + 2\mu\left(\bar{\epsilon}_{\alpha\beta} - \langle\epsilon^{(0)}_{\alpha\beta}(\mathbf{r})\rangle\right), \tag{A10}$$

and therefore the minimization condition (A9) can be read as

$$\langle\sigma_{\alpha\beta}(\mathbf{r})\rangle = 0, \tag{A11}$$

which is in agreement with the desired boundary condition of vanishing mean stress, hence

$$\bar{\epsilon}_{\alpha\beta} = \left\langle \epsilon^{(0)}_{\alpha\beta}(\mathbf{r}) \right\rangle = \hat{\epsilon}^{(0)}_{\alpha\beta}(\mathbf{k}=0). \tag{A12}$$

For the minimization of $E_2$ we represent the strain variation $\delta\epsilon_{\alpha\beta}$ through the displacement field $u_\alpha$,

$$\delta\epsilon_{\alpha\beta} = \frac{1}{2}\left(\frac{\partial u_\alpha}{\partial x_\beta} + \frac{\partial u_\beta}{\partial x_\alpha}\right), \tag{A13}$$

as the minimization has to be done with respect to $u_\alpha$ as independent degrees of freedom. Furthermore, we introduce the stress fluctuation

$$\delta\sigma_{\alpha\beta}(\mathbf{r}) = \lambda\delta_{\alpha\beta}\delta\epsilon_{\gamma\gamma}(\mathbf{r}) + 2\mu\,\delta\epsilon_{\alpha\beta}(\mathbf{r}) \tag{A14}$$

and the eigenstress

$$\sigma^{(0)}_{\alpha\beta} = \lambda\delta_{\alpha\beta}\epsilon^{(0)}_{\gamma\gamma} + 2\mu\epsilon^{(0)}_{\alpha\beta} \tag{A15}$$

as abbreviations. Then, the energy $E_2$ is minimized with respect to $u_\alpha$,

$$\frac{\delta E_2}{\delta u_\alpha} = -\frac{\partial}{\partial x_\beta}\left(\delta\sigma_{\alpha\beta}(\mathbf{r}) - \sigma^{(0)}_{\alpha\beta}(\mathbf{r})\right) = 0, \tag{A16}$$

which is the expected stress balance. In reciprocal space this relation reads

$$G^{-1}_{\alpha\beta}\hat{u}_\beta = -ik_\beta\hat{\sigma}^{(0)}_{\beta\alpha}, \tag{A17}$$

with the inverse isotropic Green tensor

$$G^{-1}_{\beta\delta} = \lambda k_\beta k_\delta + \mu k_\alpha k_\alpha \delta_{\beta\delta} + \mu k_\beta k_\delta. \tag{A18}$$

By inversion we therefore get the solution (for $\mathbf{k} \neq 0$)

$$\hat{u}_\alpha = -iG_{\alpha\gamma}k_\beta\hat{\sigma}^{(0)}_{\beta\gamma}. \tag{A19}$$

For a two-dimensional plane strain setup we get explicitly for this tensor

$$G_{2D} = \frac{1}{\mu(\lambda+2\mu)k^4} \times \begin{pmatrix} (\lambda+\mu)k_y^2 + \mu k^2 & -(\lambda+\mu)k_x k_y \\ -(\lambda+\mu)k_x k_y & (\lambda+\mu)k_x^2 + \mu k^2 \end{pmatrix}, \tag{A20}$$

with $\mathbf{k} = (k_x, k_y)$ and $k = |\mathbf{k}|$. Inserting the (general) solution into the energy expressions gives in reciprocal space by using Parseval's theorem (A4)

$$E_1 = \frac{\lambda V}{2}\sum_{\mathbf{k}\neq 0}\hat{\epsilon}^{(0)}_{\alpha\alpha}(\mathbf{k})\hat{\epsilon}^{(0)*}_{\beta\beta}(\mathbf{k}) + \mu V\sum_{\mathbf{k}\neq 0}\hat{\epsilon}^{(0)}_{\alpha\beta}(\mathbf{k})\hat{\epsilon}^{(0)*}_{\alpha\beta}(\mathbf{k}) \tag{A21}$$

and

$$\begin{aligned} E_2 = {} & \frac{\lambda V}{2}\sum_{\mathbf{k}\neq 0}\delta\hat{\epsilon}_{\alpha\alpha}(\mathbf{k})\delta\hat{\epsilon}^*_{\beta\beta}(\mathbf{k}) - \lambda V\sum_{\mathbf{k}\neq 0}\hat{\epsilon}^{(0)*}_{\alpha\alpha}(\mathbf{k})\delta\hat{\epsilon}_{\beta\beta}(\mathbf{k}) \\ & + \mu V\sum_{\mathbf{k}\neq 0}\delta\hat{\epsilon}_{\alpha\beta}(\mathbf{k})\delta\hat{\epsilon}^*_{\alpha\beta}(\mathbf{k}) \\ & - 2\mu V\sum_{\mathbf{k}\neq 0}\hat{\epsilon}^{(0)*}_{\alpha\beta}(\mathbf{k})\delta\hat{\epsilon}_{\alpha\beta}(\mathbf{k}), \end{aligned} \tag{A22}$$

using

$$\delta\hat{\epsilon}_{\alpha\beta} = \tfrac{1}{2}(ik_\alpha\hat{u}_\beta + ik_\beta\hat{u}_\alpha). \tag{A23}$$

The total elastic energy expression can then be further simplified to

$$E_{\mathrm{el}} = \frac{V}{2}\sum_{\mathbf{k}\neq 0}\left[\hat{\sigma}^{(0)*}_{\alpha\beta}(\mathbf{k})\hat{\epsilon}^{(0)}_{\alpha\beta}(\mathbf{k}) - \hat{\sigma}^{(0)}_{\alpha\gamma}(\mathbf{k})k_\alpha G_{\gamma\beta}k_\delta\hat{\sigma}^{(0)*}_{\beta\delta}(\mathbf{k})\right]. \tag{A24}$$

For case (ii), i.e., given mean strain conditions, $\bar{\epsilon}_{\alpha\beta}$ is not a degree of freedom, and therefore the variation of $E_1$ is not needed. Then we get for $E_1$

$$\begin{aligned} E_1 = {} & \frac{\lambda V}{2}\sum_{\mathbf{k}\neq 0}\hat{\epsilon}^{(0)}_{\alpha\alpha}(\mathbf{k})\hat{\epsilon}^{(0)*}_{\beta\beta}(\mathbf{k}) + \mu V\sum_{\mathbf{k}\neq 0}\hat{\epsilon}^{(0)}_{\alpha\beta}(\mathbf{k})\hat{\epsilon}^{(0)*}_{\alpha\beta}(\mathbf{k}) \\ & + \frac{\lambda V}{2}\left(\bar{\epsilon}_{\alpha\alpha} - \hat{\epsilon}^{(0)}_{\alpha\alpha}(\mathbf{k}=0)\right)^2 \\ & + \mu V\left(\bar{\epsilon}_{\alpha\beta} - \hat{\epsilon}^{(0)}_{\alpha\beta}(\mathbf{k}=0)\right)^2, \end{aligned} \tag{A25}$$

whereas $E_2$ remains unaffected. Finally, we therefore get for the total elastic energy

$$\begin{aligned} E_{\mathrm{el}} = {} & \frac{V}{2}\sum_{\mathbf{k}\neq 0}\left[\hat{\sigma}^{(0)*}_{\alpha\beta}(\mathbf{k})\hat{\epsilon}^{(0)}_{\alpha\beta}(\mathbf{k}) - \hat{\sigma}^{(0)}_{\alpha\gamma}(\mathbf{k})k_\alpha G_{\gamma\beta}k_\delta\hat{\sigma}^{(0)*}_{\beta\delta}(\mathbf{k})\right] \\ & + \frac{\lambda V}{2}\left(\bar{\epsilon}_{\alpha\alpha} - \hat{\epsilon}^{(0)}_{\alpha\alpha}(\mathbf{k}=0)\right)^2 \\ & + \mu V\left(\bar{\epsilon}_{\alpha\beta} - \hat{\epsilon}^{(0)}_{\alpha\beta}(\mathbf{k}=0)\right)^2, \end{aligned} \tag{A26}$$

which differs from case (i) only by the homogeneous contribution. Obviously, the earlier case follows from the average strain relaxation with $\hat{\epsilon}^{(0)}_{\alpha\beta}(\mathbf{k}=0) = \bar{\epsilon}_{\alpha\beta}$, in agreement with the conditions (A11) and (A12).


[1] A. Karma and W. J. Rappel, Phase-field method for computationally efficient modeling of solidification with arbitrary interface kinetics, Phys. Rev. E **53**, R3017(R) (1996).

[2] K. Wang, G. Boussinot, C. Hüter, E. A. Brener, and R. Spatschek, Modeling of dendritic growth using a quantitative nondiagonal phase field model, Phys. Rev. Mater. **4**, 033802 (2020).

[3] A. Finel, Y. Le Bouar, B. Dabas, B. Appolaire, Y. Yamada, and T. Mohri, Sharp phase field method, Phys. Rev. Lett. **121**, 025501 (2018).

[4] L.-Q. Chen, Phase-field models for microstructure evolution, Annu. Rev. Mater. Res. **32**, 113 (2002).

[5] R. Sandt, Y. Le Bouar, and R. Spatschek, Quantum annealing for microstructure equilibration with long-range elastic interactions, Sci. Rep. **13**, 6036 (2023).

[6] L. C. P. dos Santos, T. Hang, R. Sandt, M. Finsterbusch, Y. Le Bouar, and R. Spatschek, Elastic energy driven multivariant selection in martensites via quantum annealing, Phys. Rev. Res. **6**, 023076 (2024).

[7] A. B. Finnila, M. A. Gomez, C. Sebenik, C. Stenson, and J. D. Doll, Quantum annealing: A new method for minimizing multidimensional functions, Chem. Phys. Lett. **219**, 343 (1994).

[8] J. Brooke, D. Bitko, T. F. Rosenbaum, and G. Aeppli, Quantum annealing of a disordered magnet, Science **284**, 779 (1999).

[9] T. Kadowaki and H. Nishimori, Quantum annealing in the transverse Ising model, Phys. Rev. E **58**, 5355 (1998).

[10] S. Morita and H. Nishimori, Mathematical foundation of quantum annealing, J. Math. Phys. **49**, 125210 (2008).

[11] A. Rajak, S. Suzuki, A. Dutta, and B. K. Chakrabarti, Quantum annealing: An overview, Phil. Trans. R. Soc. A. **381**, 20210417 (2023).

[12] R. H. Warren, Mathematical methods for a quantum annealing computer, J. Adv. Appl. Math. **3**, 82 (2018).

[13] M. W. Johnson, M. H. Amin, S. Gildert, T. Lanting, F. Hamze, N. Dickson, R. Harris, A. J. Berkley, J. Johansson, P. Bunyk, E. M. Chapple, C. Enderud, J. P. Hilton, K. Karimi, E. Ladizinsky, N. Ladizinsky, T. Oh, I. Perminov, C. Rich, M. C. Thom, E. Tolkacheva, C. J. S. Truncik, S. Uchaikin, J. Wang, B. Wilson, and G. Rose, Quantum annealing with manufactured spins, Nature (London) **473**, 194 (2011).

[14] S. Boixo, T. F. Rønnow, S. V. Isakov, Z. Wang, D. Wecker, D. A. Lidar, J. M. Martinis, and M. Troyer, Evidence for quantum annealing with more than one hundred qubits, Nat. Phys. **10**, 218 (2014).

[15] R. Sandt and R. Spatschek, Efficient low temperature Monte Carlo sampling using quantum annealing, Sci. Rep. **13**, 6754 (2023).

[16] B. Camino, J. Buckeridge, P. A. Warburton, V. Kendon, and S. M. Woodley, Quantum computing and materials science: A practical guide to applying quantum annealing to the configurational analysis of materials, J. Appl. Phys. **133**, 221102 (2023).

[17] R. Harris, Y. Sato, A. J. Berkley, M. Reis, F. Altomare, M. H. Amin, K. Boothby, P. Bunyk, C. Deng, C. Enderud, S. Huang, E. Hoskinson, M. W. Johnson, E. Ladizinsky, N. Ladizinsky, T. Lanting, R. Li, T. Medina, R. Molavi, R. Neufeld, T. Oh, I. Pavlov, I. Perminov, G. Poulin-Lamarre, C. Rich, A. Smirnov, L. Swenson, N. Tsai, M. Volkmann, J. Whittaker, and J. Yao, Phase transitions in a programmable quantum spin glass simulator, Science **361**, 162 (2018).

[18] P. Kairys, A. D. King, I. Ozfidan, K. Boothby, J. Raymond, A. Banerjee, and T. S. Humble, Simulating the Shastry-Sutherland Ising model using quantum annealing, PRX Quant. **1**, 020320 (2020).

[19] K. Kitai, J. Guo, S. Ju, S. Tanaka, K. Tsuda, J. Shiomi, and R. Tamura, Designing metamaterials with quantum annealing and factorization machines, Phys. Rev. Res. **2**, 013319 (2020).

[20] J. Nelson, M. Vuffray, A. Y. Lokhov, T. Albash, and C. Coffrin, High-quality thermal gibbs sampling with quantum annealing hardware, Phys. Rev. Appl. **17**, 044046 (2022).

[21] M. Vuffray, C. Coffrin, Y. A. Kharkov, and A. Y. Lokhov, Programmable quantum annealers as noisy gibbs samplers, PRX Quant. **3**, 020317 (2022).

[22] S. Mandrà, Z. Zhu, and H. G. Katzgraber, Exponentially biased ground-state sampling of quantum annealing machines with transverse-field driving Hamiltonians, Phys. Rev. Lett. **118**, 070502 (2017).

[23] M. S. Könz, G. Mazzola, A. J. Ochoa, H. G. Katzgraber, and M. Troyer, Uncertain fate of fair sampling in quantum annealing, Phys. Rev. A **100**, 030303(R) (2019).

[24] S. Mukherjee and B. K. Chakrabarti, On the question of ergodicity in quantum spin glass phase and its role in quantum annealing, J. Phys. Soc. Jpn. **88**, 061004 (2019).

[25] M. Yamamoto, M. Ohzeki, and K. Tanaka, Fair sampling by simulated annealing on quantum annealer, J. Phys. Soc. Jpn. **89**, 025002 (2020).

[26] M. Jünger, E. Lobe, P. Mutzel, G. Reinelt, F. Rendl, G. Rinaldi, and T. Stollenwerk, Quantum annealing versus digital computing: An experimental comparison, ACM J. Exp. Algorithm. **26**, 1 (2021).

[27] O. Parekh, J. Wendt, L. Shulenburger, A. Landahl, J. Moussa, and J. Aidun, Benchmarking adiabatic quantum optimization for complex network analysis, https://www.osti.gov/biblio/1459086 (2015).

[28] B. Yan and N. A. Sinitsyn, Analytical solution for nonadiabatic quantum annealing to arbitrary Ising spin Hamiltonian, Nat. Commun. **13**, 2212 (2022).

[29] A. D. King, J. Raymond, T. Lanting, R. Harris, A. Zucca, F. Altomare, A. J. Berkley, K. Boothby, S. Ejtemaee, C. Enderud, E. Hoskinson, S. Huang, E. Ladizinsky, A. J. R. MacDonald, G. Marsden, R. Molavi, T. Oh, G. Poulin-Lamarre, M. Reis, C. Rich, Y. Sato, N. Tsai, M. Volkmann, J. D. Whittaker, J. Yao, A. W. Sandvik, and M. H. Amin, Quantum critical dynamics in a 5, 000-qubit programmable spin glass, Nature (London) **617**, 61 (2023).

[30] R. Y. Li, R. Di Felice, R. Rohs, and D. A. Lidar, Quantum annealing versus classical machine learning applied to a simplified computational biology problem, npj Quantum Inf. **4**, 14 (2018).

[31] A. Perdomo-Ortiz, N. Dickson, M. Drew-Brook, G. Rose, and A. Aspuru-Guzik, Finding low-energy conformations of lattice protein models by quantum annealing, Sci. Rep. **2**, 571 (2012).

[32] A. Irbäck, L. Knuthson, S. Mohanty, and C. Peterson, Folding lattice proteins with quantum annealing, Phys. Rev. Res. **4**, 043013 (2022).

[33] E. Boyda, S. Basu, S. Ganguly, A. Michaelis, S. Mukhopadhyay, and R. R. Nemani, Deploying a quantum annealing processor to detect tree cover in aerial imagery of California, PLoS ONE **12**, e0172505 (2017).

[34] F. Neukart, G. Compostella, C. Seidel, D. von Dollen, S. Yarkoni, and B. Parney, Traffic flow optimization using a quantum annealer, Front. ICT **4**, 29 (2017).

[35] M. Ohzeki, A. Miki, M. J. Miyama, and M. Terabe, Control of automated guided vehicles without collision by qantum annealer and digital devices, Front. Comput. Sci. **1**, 9 (2019).

[36] L. Mañosa and A. Planes, Mechanocaloric effects in shape memory alloys, Phil. Trans. R. Soc. A. **374**, 20150310 (2016).

[37] K. Otsuka and X. Ren, Physical metallurgy of Ti–Ni-based shape memory alloys, Prog. Mater. Sci. **50**, 511 (2005).

[38] D. Sherrington, A simple spin glass perspective on martensitic shape-memory alloys, J. Phys.: Condens. Matter **20**, 304213 (2008).

[39] S. Kartha, T. Castán, J. A. Krumhansl, and J. P. Sethna, Spin-Glass nature of tweed precursors in martensitic transformations, Phys. Rev. Lett. **67**, 3630 (1991).

[40] J. P. Sethna, S. Kartha, T. Castán, and J. A. Krumhansl, Tweed in Martensites: A potential new spin glass, Phys. Scr. **T42**, 214 (1992).

[41] R. Vasseur and T. Lookman, Spin models for ferroelastics: Towards a spin glass description of strain glass, Solid State Phenom. **172-174**, 1078 (2011).

[42] C. A. Geiger, E. Alekseev, B. Lazic, M. Fisch, T. Armbruster, R. Langner, M. Fechtelkord, N. Kim, T. Pettke, and W. Weppner, Crystal chemistry and stability of "$Li_7La_3Zr_2O_{12}$" garnet: A fast lithium-ion conductor, Inorg. Chem. **50**, 1089 (2011).

[43] E. Enkhbayar and J. H. Kim, Study of codoping effects of $Ta^{5+}$ and $Ga^{3+}$ on Garnet $Li_7La_3Zr_2O_{12}$, ACS Omega **7**, 47265 (2022).

[44] L. J. Miara, S. P. Ong, Y. Mo, W. D. Richards, Y. Park, J.-M. Lee, H. S. Lee, and G. Ceder, Effect of Rb and Ta doping on the ionic conductivity and stability of the garnet $Li_{7+2x-y}$ $(La_{3-x}Rb_x)$ $(Zr_{2-y}Ta_y)$ $O_{12}$ $(0 \leqslant x \leqslant 0.375, 0 \leqslant y \leqslant 1)$ Superionic Conductor: A first principles investigation, Chem. Mater. **25**, 3048 (2013).

[45] H. Buschmann, J. Dölle, S. Berendts, A. Kuhn, P. Bottke, M. Wilkening, P. Heitjans, A. Senyshyn, H. Ehrenberg, A. Lotnyk, V. Duppel, L. Kienle, and J. Janek, Structure and dynamics of the fast lithium ion conductor $Li_7La_3Zr_2O_{12}$, Phys. Chem. Chem. Phys. **13**, 19378 (2011).

[46] S. Yu, R. D. Schmidt, R. Garcia-Mendez, E. Herbert, N. J. Dudney, J. B. Wolfenstine, J. Sakamoto, and D. J. Siegel, Elastic properties of the solid electrolyte $Li_7La_3Zr_2O_{12}$ (LLZO), Chem. Mater. **28**, 197 (2016).

[47] J. F. Nonemacher, C. Hüter, H. Zheng, J. Malzbender, M. Krüger, R. Spatschek, and M. Finsterbusch, Microstructure and properties investigation of garnet structured $Li_7La_3Zr_2O_{12}$ as electrolyte for all-solid-state batteries, Solid State Ion. **321**, 126 (2018).

[48] R. Sandt, Y. Wang, and R. Spatschek, Investigation of mechanical properties of garnet structured $Li_7La_3Zr_2O_{12}$ under $Al^{3+}$ and $Ta^{5+}$ co-substitutions, Solid State Ion. **402**, 116364 (2023).

[49] W. C. Johnson and P. W. Voorhees, Elastic interactions and stability of misfitting cuboidal inhomogeneities, J. Appl. Phys. **61**, 1610 (1987).

[50] C. H. Rycroft, VORO++: A three-dimensional Voronoi cell library in C++, Chaos **19**, 041111 (2009).

[51] F. Aurenhammer, Voronoi diagrams—A survey of a fundamental geometric data structure, ACM Comput. Surv. **23**, 345 (1991).

[52] J. Raymond, R. Stevanovic, W. Bernoudy, K. Boothby, C. C. McGeoch, A. J. Berkley, P. Farré, J. Pasvolsky, and A. D. King, Hybrid quantum annealing for larger-than-QPU lattice-structured problems, ACM Trans. Quantum Comput. **4**, 1 (2023).

[53] V. Choi, Minor-embedding in adiabatic quantum computation: II. Minor-universal graph design, Quant. Inf. Process. **10**, 343 (2011).

[54] J. J. Berwald, The mathematics of quantum-enabled applications on the D-Wave quantum computer, Not. Am. Math. Soc. **66**, 832 (2019).

[55] D-Wave Leap quantum cloud service, https://cloud.dwavesys.com.

[56] H.-C. Yu, D. Taha, T. Thompson, N. J. Taylor, A. Drews, J. Sakamoto, and K. Thornton, Deformation and stresses in solid-state composite battery cathodes, J. Power Sources **440**, 227116 (2019).

[57] https://www.fz-juelich.de/ias/jsc.

[58] M. Frigo and S. G. Johnson, The design and implementation of FFTW3, Proc. IEEE **93**, 216 (2005).

[59] A. G. Khachaturyan, *Theory of Structural Transformations in Solids* (Dover Publications, Mineola, NY, 2008).